Determination of three-dimensional cloud structures from high-resolution radiance data

T. Zinner,[1] B. Mayer,[1] and M. Schröder[2]

Received 11 April 2005; revised 8 July 2005; accepted 13 January 2006; published 26 April 2006.

[1] The three-dimensional structure and the inhomogeneity of clouds pose a field of challenges. The characterization of their spatial structure, their microphysical properties, and their variability is difficult. This kind of knowledge is crucial to any investigation on the impact of clouds on the radiation budget or on the reliability of cloud remote sensing data. In this article the characteristics of radiation transport in inhomogeneous clouds are studied using three-dimensional (3-D) simulations of radiative transport and the independent pixel approximation (IPA). The opposing effects of radiative smoothing and sharpening due to horizontal photon transport are examined in terms of the Green's function, which describes the interrelation of the radiance fields calculated using IPA and 3-D radiative transport. On the basis of these considerations a novel method was developed for the retrieval of realistic 3-D stratocumulus structures from high-spatial-resolution radiance fields observed by a compact airborne spectrographic imager (CASI, 15 m resolution). An initial distribution of liquid water content and effective droplet size retrieved using the IPA assumption and an adiabatic microphysical model is iteratively adjusted with the objective of matching the observation by the 3-D forward radiative transfer simulation for the derived cloud. For the iterative adjustment an approximate Green's function is utilized to remove 3-D effects from the observation. The performance of the method is characterized by application to a known cloud structure and by comparison of the derived cloud properties to in situ data from various field campaigns. The method provides the ideal basis for our studies on the remote sensing of inhomogeneous clouds.

Citation: Zinner, T., B. Mayer, and M. Schröder (2006), Determination of three-dimensional cloud structures from high-resolution radiance data, *J. Geophys. Res.*, *111*, D08204, doi:10.1029/2005JD006062.

1. Introduction

[2] Clouds are three-dimensional and highly inhomogeneous on all scales of time and space. That causes a variety of problems for the measurement of cloud properties, in particular for passive remote sensing techniques. At the same time, our knowledge of cloud characteristics and their evolution in time decisively depends on passive remote sensing from space and aircraft as only those can provide sufficiently complete data sets in terms of horizontal coverage. Future active remote sensing instruments like CloudSat and Calipso [*Stephens et al.*, 2002] will give new insights and complement the passive measurements.

[3] As the horizontal resolution of a sensor is always limited, the lack of information on subpixel-scale variability leads to the basic assumption of standard remote sensing: Clouds are assumed to be plane-parallel and homogeneous throughout the field of view of the instrument. This is the plane parallel approximation (PPA). This assumption causes a bias in the retrieved cloud parameters due to the nonlinear dependence of cloud properties and the related reflected radiance, the so-called plane-parallel bias [*Cahalan et al.*, 1994a]. The plane parallel bias generally increases with pixel size as the amount of subscale inhomogeneity is increasing. A second assumption is generally used by remote sensing algorithms: Individual pixels are considered independent. This is the so-called independent pixel approximation (IPA). The IPA neglects net horizontal transport of radiation between neighboring pixels, which causes the so-called independent pixel error [*Cahalan et al.*, 1994b]. The independent pixel error increases as the pixel size decreases because the smaller the pixel is the more important is the net horizontal photon transport compared to the vertical transport.

[4] Apart from several investigations on the impact of a neglect of cloud inhomogeneity and three-dimensional (3-D) radiative transport on the derived radiative fluxes [e.g., *Cahalan et al.*, 1994a, 1994b; *Marshak et al.*, 1998c; *Fu et al.*, 2000; *Scheirer and Macke*, 2003; *Di Giuseppe and Tompkins*, 2003], there have been first attempts to investigate the uncertainties of cloud property retrievals [*Loeb et al.*, 1998; *Varnai*, 2000] and to systematically

[1] Institut für Physik der Atmosphäre, Deutsches Zentrum für Luft- und Raumfahrt Oberpfaffenhofen, Weßling, Germany.
[2] Institut für Weltraumwissenschaften, Freie Universität Berlin, Berlin, Germany.

0148-0227/06/2005JD006062$09.00

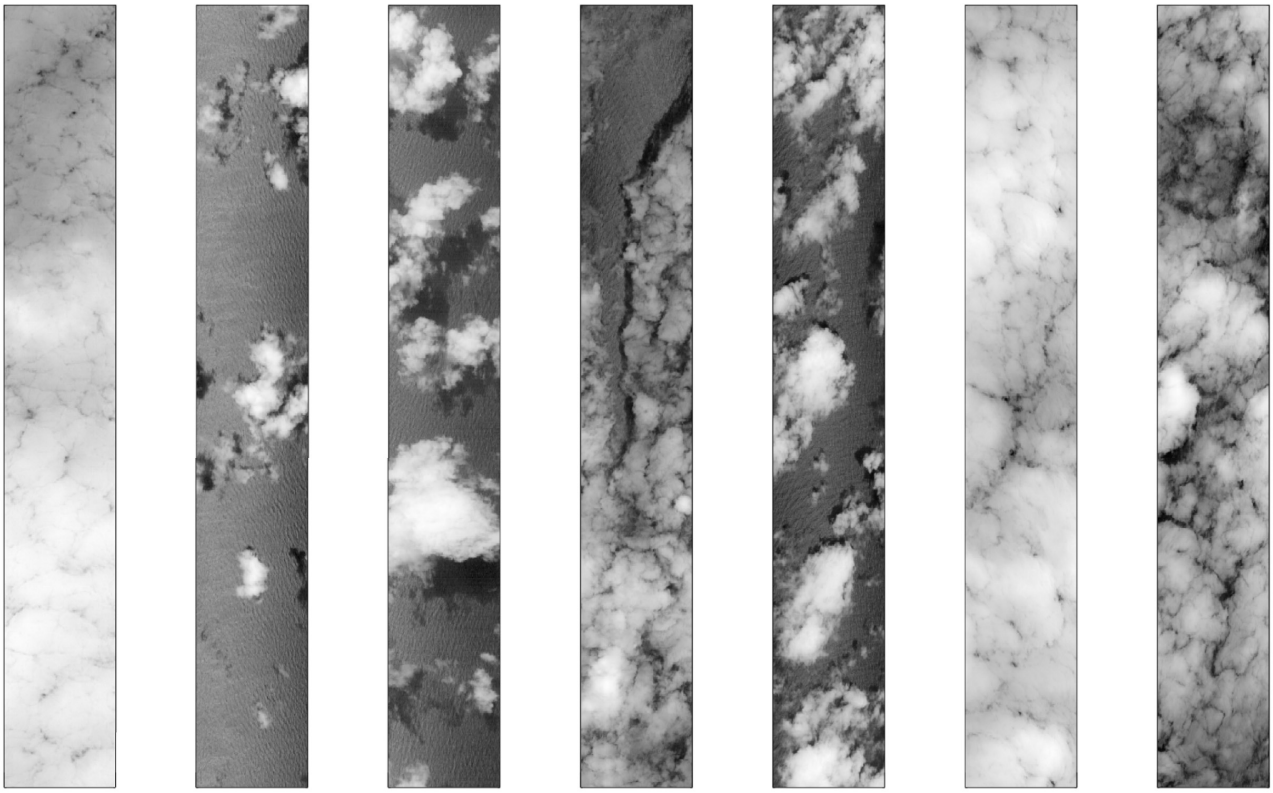

Figure 1. Examples of CASI observations: radiance at 753 nm, horizontal resolution 15 m × 15 m, scene size approximately 1.3 km × 10 km, boundary layer clouds over ocean, north of the Canary Islands, June/July 1997. The resolution is high enough to observe waves at the ocean surface.

quantify them [*Varnai and Marshak*, 2001]. First approaches to quantitatively consider cloud inhomogeneity in retrieval schemes were proposed as well [*Faure et al.*, 2001, 2002; *Iwabuchi and Hayasaka*, 2003].

[5] The influence of cloud variability and 3-D radiative transport on remote sensing cannot be quantified on the basis of passive remote sensing data only since the true cloud properties remain unknown [*Cahalan et al.*, 1994a; *Coakley*, 1991; *Rossow et al.*, 2002]. Thus most of the aforementioned analyses and methods were based on a priori defined 3-D cloud structures (3-D distributions of liquid water content (LWC) and cloud particle size distributions) which were used as input to realistic 3-D radiative transport simulations. Consequently all approaches depend on the complexity and the realism of the underlying cloud structures.

[6] In addition to statistical cloud models, first attempts have been made to use physics-based cloud simulation data (e.g., from large eddy simulations) as input to similar investigations [*O'Hirok and Gautier*, 1998; *Scheirer and Macke*, 2003; *Wyser et al.*, 2002; *Barker et al.*, 2003]. The preparation of such data sets is computationally expensive; on the other hand their realism is still doubtable, especially as far as the small-scale variability of cloud microphysics is concerned as it is affected by numerical filtering [*Bryan et al.*, 2003]. Generally, it seems desirable to stay as close as possible to observed data. This is for example achieved with the aid of sophisticated statistical cloud models extrapolating observed characteristics of the cloud microphysics to full 3-D structures. Starting from in situ measurements [*Venema et al.*, 2004; *Scheirer and Schmidt*, 2005] or radar cross sections [*Evans and Wiscombe*, 2004], large information gaps have to be filled because of the limited spatial sampling achievable today.

[7] This paper introduces a method to determine 3-D cloud structures directly from observations and thereby to ensure that the basic features of a cloud scene and the natural variability of cloud situations are obtained. For this purpose a novel remote sensing method to derive complete 3-D cloud structures from high-resolution radiance fields measured by an airborne spectrometer is described. This method quantitatively takes into account 3-D radiative transport. Section 2 introduces the basic ideas. In section 3 the details of the method and of the generated cloud data sets' are given; the cloud properties are summarized and compared to different measurements of typical properties of marine stratocumulus. In section 4 a test of the method is shown using an artificial test case. In sections 5 and 6 the capabilities and limitations of the method are discussed and an outlook on possible refinements and applications is given.

2. Basis

2.1. Data

[8] The data basis of high-horizontal-resolution radiance observations is provided by the compact airborne spectrographic imager (CASI) [*Babey and Anger*, 1989]. The CASI is a "push broom" imaging spectrometer with a field of view of 34° across the flight track. The data was collected over sea on board the DLR Do-228 aircraft during the ACE2

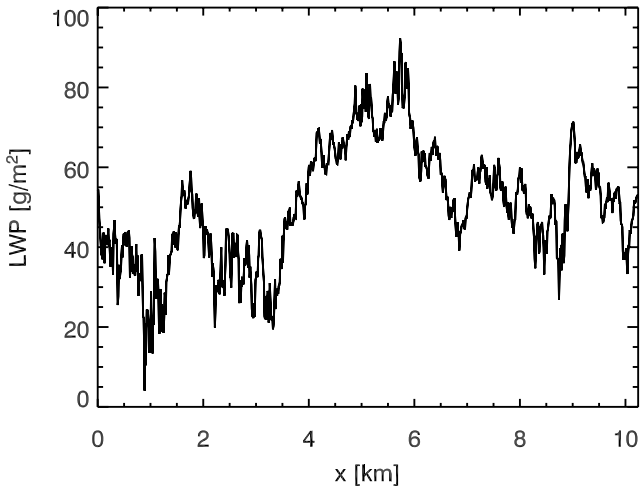

Figure 2. Distribution of liquid water path (LWP) of a cloud structure with a power spectral behavior of −5/3.

CLOUDYCOLUMN campaign north of the Canary Islands in June/July 1997. Here data from the scene recovery channel operated at 753 nm is used, which provides the full resolution of 512 cross-track pixels corresponding to a spatial resolution of about 2.5 m at cloud top. The along-track resolution of 15 m results from the aircraft speed and the sampling time of the instrument. The cross track resolution of 2.5 m is reduced to yield approximately quadratic pixels of 15 m × 15 m. Twenty-seven cases of marine stratocumulus observations at solar zenith angles between 6.5° and 16° were selected. The cases comprise cloud fractions between 5 and 100% (Figure 1). All scenes are of similar size of about 1.3 km × 10 km. Some auxiliary information (in situ measurements of number densities of droplets or cloud condensation nuclei) is taken from publications on the ACE2 CLOUDYCOLUMN campaign [*Brenguier et al.*, 2000b; *Chuang*, 2000].

2.2. Radiative Transfer Models

[9] For all following simulations of radiative transport the 3-D Monte Carlo code MYSTIC validated in the intercomparison of 3-D radiation codes (I3RC) [*Mayer*, 1999, 2000; *Cahalan et al.*, 2005] is used. To achieve complete consistency, even the calculation of IPA reflectivities in section 2.3 as well as the preparation of a lookup table for a standard IPA retrieval of optical thickness are done with the 3-D MYSTIC in IPA mode where the horizontal transport of photons between columns is switched off. The model is part of the libRadtran (library of radiative transfer) package [*Mayer and Kylling*, 2005]. For an adequate simulation of the CASI measurement, a Lambertian surface albedo of 2.5% (realistic outside the sunglint region) is assumed and all simulations are done monochromatically at 753 nm. Cloud microphysical parameters are converted to optical properties via Mie calculations. For all calculations a standard atmosphere for midlatitude summer was assumed [*Anderson et al.*, 1986].

2.3. Basic Ideas

[10] As for each remote sensing instrument, the mentioned uncertainties, the plane-parallel (PP) bias and the independent pixel (IP) error, have to be considered when evaluating the CASI observations. At a resolution of 15 m × 15 m the PP bias can be assumed to vanish as no significant subscale variability of the radiation field has to be expected below this scale. *Marshak et al.* [1998b] state the critical scale to be the mean free path length of photons between two scattering or absorption events. For the cloud scenes investigated here this value is typically larger than 15 m. In contrast, the IP error introduced by horizontal photon transport is certainly of decisive importance to remote sensing methods at this resolution. The problem to be solved is the search for the 3-D cloud structure whose related radiance field matches the observed distribution. In order to complete this task the basic physical processes of radiative transport need to be accounted for.

[11] Following *Marshak et al.* [1998a], the horizontal transport of photons can be described by means of a Green's function. This function is the link between the 3-D radiance field and the IPA radiance field and depends mainly on the optical thickness, the geometrical thickness, and the scattering asymmetry factor. Knowledge of the Green's function would in principle allow the retrieval of the correct cloud properties with the usual IPA, as the actual observed 3-D field could be deconvolved to yield the IPA field. In real applications, however, neither the Green's function nor the IPA radiance field are known.

[12] The IPA and the 3-D radiance fields can be calculated via radiative transfer simulations, if the underlying cloud field is known. Both radiance fields simulated for a given cloud case (Figure 2) are displayed in Figure 3. The cloud structure has been generated using a statistical model employing a rescaling of a random distribution of liquid water path (LWP) values to fit the −5/3 power law [*Kolmogorov*, 1941], similar to the models described by *Di Giuseppe and Tompkins* [2003] and *Venema et al.* [2004]. The data series shown in Figure 2 represents the variability of the cloud LWP between fixed cloud base and top heights and comprises a typical range of values for marine stratocumulus: the liquid water path reaches values of up to 90 g/m^2 corresponding to an optical thickness of 15. The related fields of nadir ($\theta_{sensor} = 0°$) reflectivity for a zenith Sun ($\theta_{sun} = 0°$) in Figures 3a and 3b are simulated in IPA mode and 3-D mode, respectively. There is an obvious difference between the 3-D and IPA reflectivity fields, called the radiative smoothing effect [*Marshak et al.*, 1995; *Davis et al.*, 1997]. This effect is caused by the horizontal diffusion of photons which occurs only in the 3-D calculation. The 3-D field can be described as the convolution of the IPA field with the Green's function. Given the two simulated fields the Green's function can thus be determined from the 3-D and IPA reflectivity fields. This is best done in Fourier space where a convolution corresponds to a simple multiplication of Fourier series. Figure 3c shows the Fourier space picture, i.e., the power spectra of the three data series of LWP, IPA reflectivity, and 3-D reflectivity. While the IPA spectrum follows the −5/3 slope that was used to generate the LWP field, the amplitudes of the 3-D spectrum for higher wave numbers k are smaller because of the smoothing of high frequencies in the reflectivity fields. It should be mentioned at this point that such a change of smoothing regimes, marked by a power spectral scale break, was found in analyses of satellite and airborne

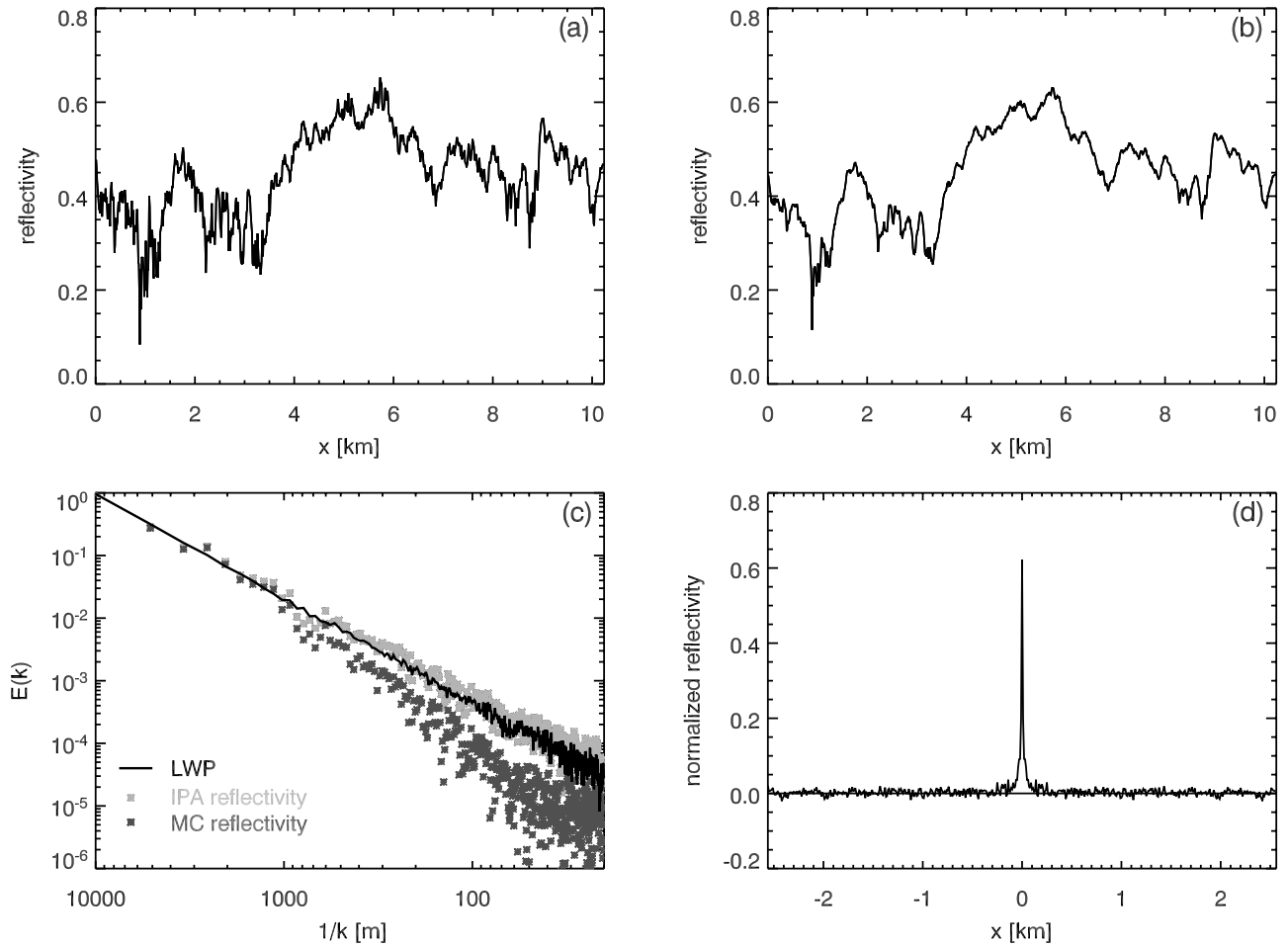

Figure 3. (a) Top-of-atmosphere IPA reflectivity from DISORT simulations for the LWP field in Figure 2 (constant cloud base and top), (b) 3-D reflectivity from MYSTIC simulations for $\theta_{sun} = 0°$, $\theta_{sensor} = 0°$, (c) power spectra for LWP, IPA, and 3-D reflectivity fields, and (d) corresponding Green's function.

data before and was related to horizontal photon transport at the scale of cloud geometrical thickness h (here $h = 200$ m) [*Marshak et al.*, 1995, 1998a; *Davis et al.*, 1997; *Schröder and Bennartz*, 2003]. In the investigated example a change of slope is visible at about 1000 m. The Green's function obtained via division of the Fourier series of the 3-D by the IPA reflectivity field and back transformation into real space is depicted in Figure 3d. A plain analog to the Green's function is the reflection function of a laser beam entering the cloud from the top which would produce a similar reflectivity distribution because its light is transported away from the entry point before it eventually leaves the cloud at the top.

[13] A more realistic description of a cloud should include cloud top structure. To introduce cloud top height variability, we translate each value of the LWP distribution to a geometrical cloud thickness using an adiabatic microphysical model. The liquid water content of an air parcel is assumed to grow with height according to the adiabatic LWC which can be calculated assuming adiabatic lifting of a saturated air parcel. Depending on the cloud base height and the liquid water path a cloud top structure is generated (further details in Appendix A). Figure 4 shows the results for this cloud case. Now a contrary effect of the horizontal photon transport becomes effective: the radiative sharpening effect [*Loeb et al.*, 1998; *Varnai*, 2000]. The sharpening is typically caused by cloud side illumination and shadows. Although hardly detectable in the reflectivity picture the partial statistical compensation of the smoothing effect can be seen in the power spectrum by the increase of amplitudes at high wave numbers. Although sharpening effects obviously become more relevant for low Sun, they also occur for overhead Sun because a certain fraction of the radiation is always dispersed in the top parts of the cloud providing a horizontal component. This effect is enhanced for larger solar zenith angles, e.g., for $\theta_{sun} = 30°$ in Figure 5. Then shadows and bright slopes lead to a much rougher appearance of the reflectivity distribution than it is the case for the IPA field. The sharpening is reflected in the power spectra by larger amplitudes at all but the lowest frequencies. The Green's function is much more complex now. Its distinct negative values reflect the shadow effects: For example, a high value in the IPA field is not necessarily related to a bright 3-D pixel anymore, because the latter is rather a sign of a sunlit slope than of a high optical thickness. As the Green's function displayed is the combination of the horizontal transport characteristic of any pixel's surrounding in the field (which in case of strong shadowing is very distinct for each point) a simple relationship to the features of the involved fields (3-D, IPA) is not to be expected.

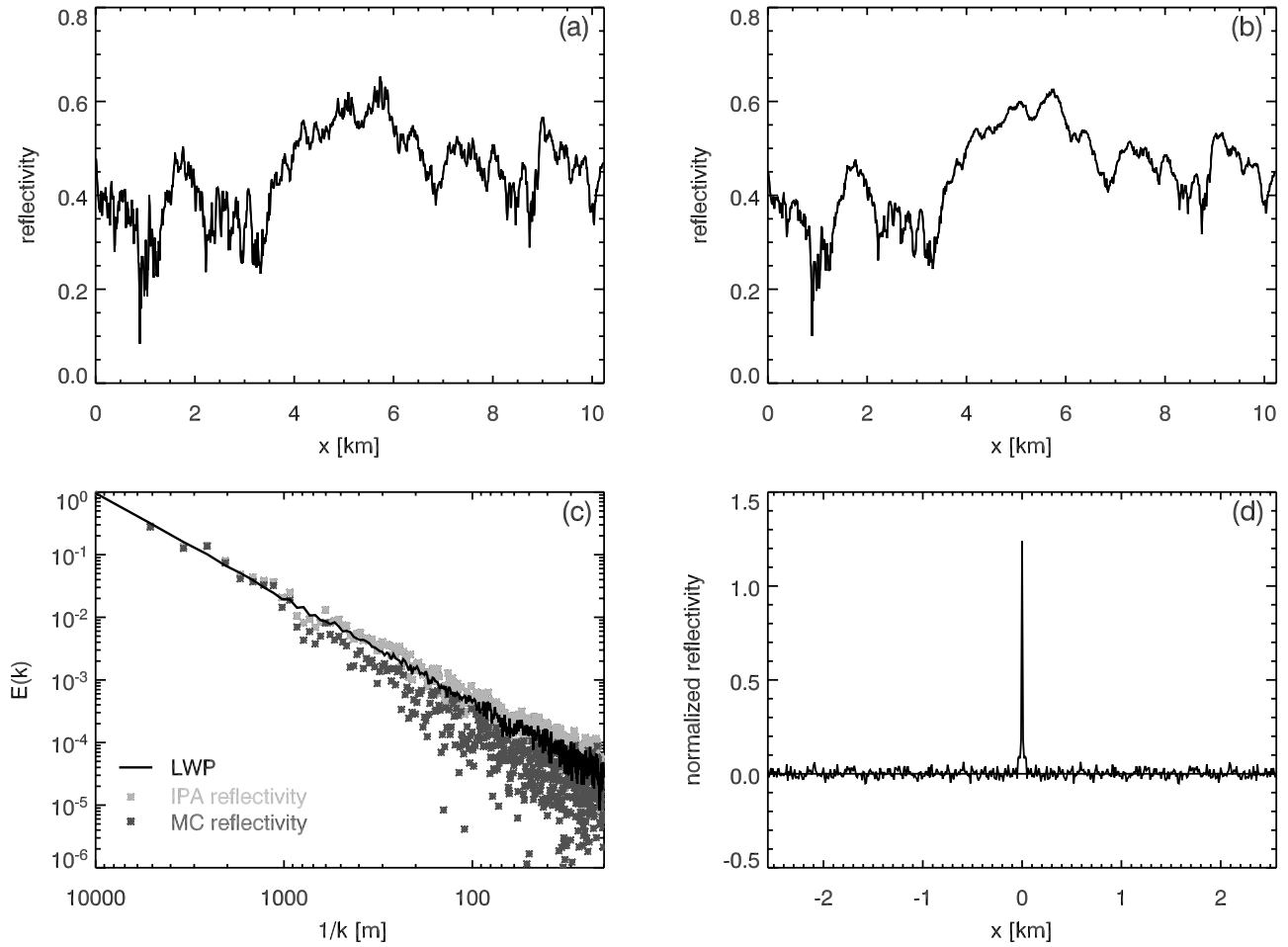

Figure 4. Same as Figure 3, but for variable cloud top height.

[14] On the basis of the characteristics of radiative smoothing, *Marshak et al.* [1998a] propose the "nonlocal independent pixel approximation" to correct a retrieval of cloud properties for the influence of horizontal transport phenomena: An observed (3-D) radiance field can be deconvolved with a Green's function prior to the application of standard remote sensing techniques to the resulting IPA field. This technique of course requires knowledge of the true Green's function for the specific cloud field. It can be shown that a Green's function obtained as shown before can be used to improve the retrieval for similar cloud fields, if the clouds lack cloud top structure as in the study by *Marshak et al.* [1998a]. On the contrary this approach fails if cloud top structure and nonzenith Sun is introduced and thus radiative sharpening becomes more important. In that case the Green's function is very specific for a given cloud case. In contrast to radiative smoothing which is mainly depending on the average values of a cloud area like the average optical and geometrical thickness, radiative sharpening is highly sensitive to the small-scale local geometry deciding if a pixel is illuminated or shaded. Thus the Green's function for a certain cloud scene contains all these detailed information and is not applicable to other scenes anymore.

[15] Nonetheless, the Green's function or, as its approximations are called from here on, the "point spread function" (PSF) constitutes the core of the method introduced in this paper. Although the true Green's function is unknown for a given observed reflectivity field (i.e., it is unknown to which extent radiative smoothing and sharpening act in the first place) it can be safely assumed that in case of small solar zenith angles the smoothing dominates the sharpening (visible in Figures 3b, 4b, and 5b). The smoothing effect is defined by the mean free path of photons in the cloud which does not change significantly with zenith angle. The sharpening becomes more significant for larger solar zenith angles with increasing shadow effects until at the largest zenith angles the contrasts become smoother again as major parts of the cloud scene are shadowed then. Hence a stepwise deconvolution with an approximate PSF will be applied to selected scenes observed at small solar zenith angles. This way an incomplete deconvolution is possible and thus a partial compensation of radiative smoothing by sharpening effects can be considered. An objective criterion is established to stop the deconvolution at the appropriate point, by comparing the observed radiance field with a 3-D simulation based on the derived cloud structure.

3. Method

[16] As discussed a prerequisite is the selection of appropriate CASI scenes. All of the selected 27 scenes have been observed between 1130 and 1310 local time. Thus the solar zenith angle was smaller than 16°. Using a single wave-

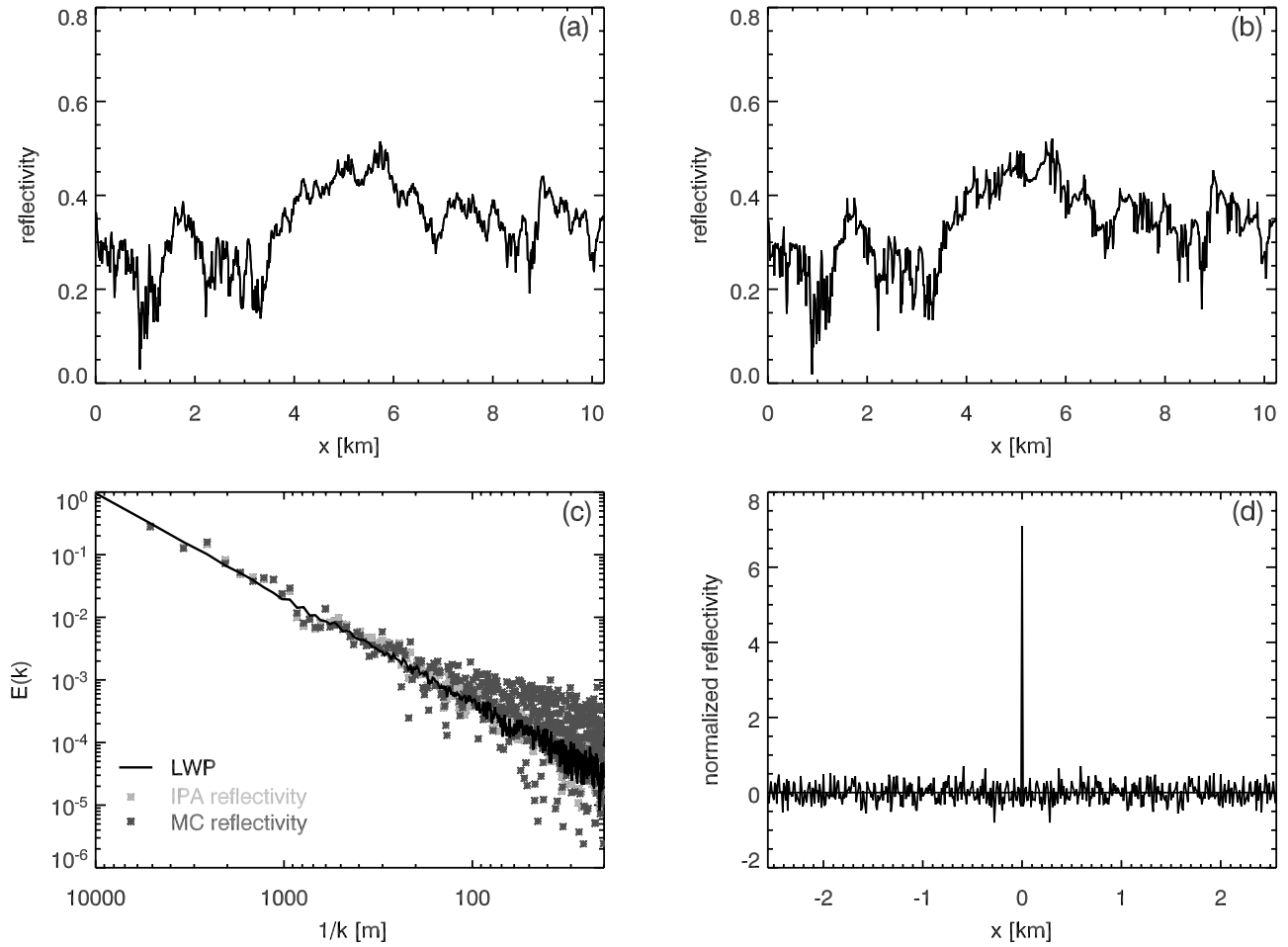

Figure 5. Same as Figure 3, but for variable cloud top height and $\theta_{sun} = 30°$.

length, cloud optical thickness and via the adiabatic assumption (Appendix A) geometrical thickness as well as effective droplet size are retrieved for each pixel under the independent pixel and plane-parallel assumptions (IPA retrieval). A point spread function is determined by calculating the spread of a laser beam in a plane parallel cloud generated by horizontally averaging the derived cloud properties over the domain. This function is used to deconvolve the observed radiance fields (section 3.2). As only mean scene properties are used and neither the specific variations of cloud properties nor cloud top height are considered, this PSF represents only the smoothing component. Thus a complete deconvolution with this PSF would overestimate the actual smoothing effect as it neglects the counteracting sharpening effects. Iterative deconvolution methods allow an incomplete deconvolution because they may be stopped after a number of iteration steps. An established iterative method, the Richardson-Lucy algorithm, is therefore used for the stepwise deconvolution of the observed radiance field to obtain several versions of the initial observation with increasing roughness. For each of these, the full cloud structure is retrieved using the described IPA procedure, including an adiabatic assumption of the vertical structure (section 3.3). For these structures, in turn, the radiance for the Sun and sensor geometry of the related observation is simulated with the 3-D MYSTIC model (section 3.4). Finally, criteria have to be found to select the 3-D cloud structure best matching the CASI observation (section 3.5). In other words, a first guess cloud structure is determined from the observation and subsequently adjusted until the 3-D radiation field calculated for the cloud structure resembles the original CASI observation.

3.1. Independent Pixel Retrieval

[17] As a first step, the 2-D distributions of optical and geometrical thickness are determined from the observation. Therefore a lookup table with the tabulated relation of optical thickness and radiance at 753 nm is used to retrieve an IPA of the cloud properties for each pixel separately. The mean cloud geometrical thickness results from the adiabatic assumption. Thus the optical thickness is linked to geometrical thickness, if the droplet size distribution or the according effective droplet radius is known. The latter is estimated from the LWC using fixed cloud droplet densities taken from publications on the ACE2 CLOUDYCOLUMN campaign [*Brenguier et al.*, 2000b; *Chuang*, 2000]. Mean scene cloud properties are derived by averaging all values of cloudy pixels.

3.2. Determination of an Approximate Green's Function

[18] Figure 6 presents the result of a special "laser-like" MYSTIC simulation where all photons enter a plane-parallel cloud layer from the zenith direction at the central point

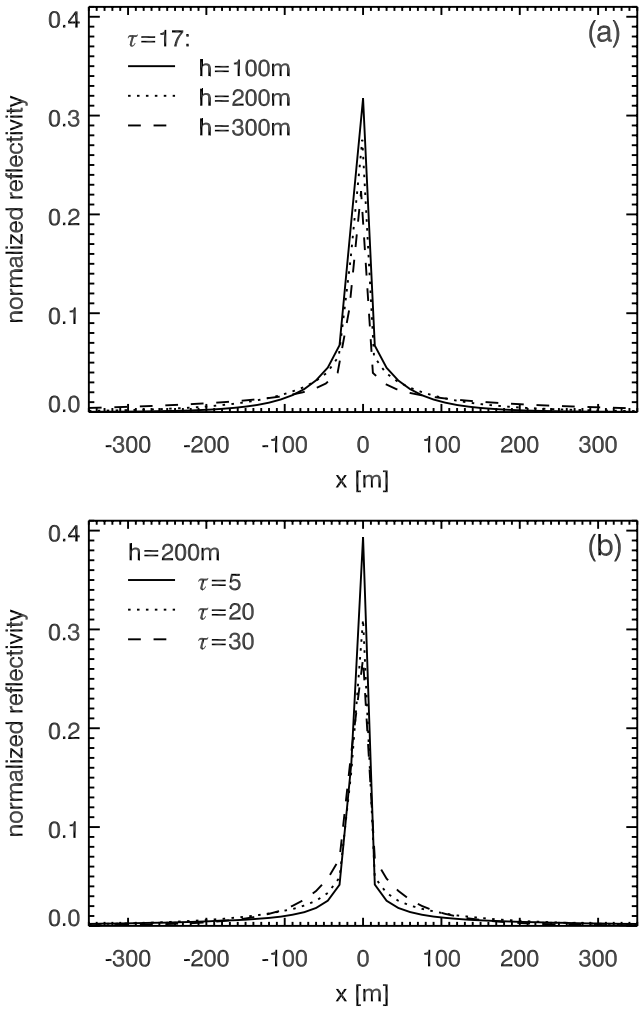

Figure 6. (a) Point spread function from "laser-like" MYSTIC simulations for a plane-parallel cloud layer $\tau = 17$ and h = 100, 200, 500 m. The central pixel at $x = 0$ is illuminated from zenith $\theta_{sun} = 0°$. (b) Same as Figure 6a but for h = 200 m and τ = 5, 10, 30.

of the field. The distribution of the photons reflected back toward zenith after a number of scattering events displays the effect of horizontal photon transport. As already mentioned above, this function mainly depends on the geometrical thickness h, on the optical thickness τ, and on the asymmetry parameter [*Marshak et al.*, 1998a]. In fact, lidar systems based on this idea are already used to determine the geometrical thickness of clouds [*Davis et al.*, 1999].

[19] It might seem possible to find a better approximation of the Green's function by using the, at least approximately, available two-dimensional distribution of cloud properties and subsequent simulations similar to the method shown in section 2.3. Feasible for small synthetic 1-D fields there, it is not feasible to determine meaningful approximations for the large CASI 2-D fields this way. The prerequisite for such a determination would be noise-free fields: Neither the original measurement is noise-free nor can any subsequent 3-D simulation be close to noise-free without great computational effort.

[20] Here the point spread function is determined according to the mentioned dependencies on optical and geometrical thickness. According to the mean values of geometrical and optical thickness and effective droplet size identified before, the point spread function is simulated with MYSTIC (Figure 6) for a plane parallel cloud layer comprising the mean characteristics. This way a deconvolution kernel is found which contains the average radiative smoothing characteristics of the specific cloud field. Of course, this comprises neither local characteristics of horizontal photon transport nor any sharpening effects. Thus a complete deconvolution of an observed radiance distribution with this PSF would lead to an overcompensation of horizontal transport. Therefore an iterative deconvolution terminated at a certain step is a logical consequence.

3.3. Iterative Deconvolution Algorithm

[21] Deconvolution problems without the knowledge of the exact convolution function, so-called "blind" deconvolutions, are usually solved with the aid of iterative approaches which are terminated according to certain criteria. A standard algorithm for such tasks is the Richardson-Lucy algorithm independently developed by *Richardson* [1972] and *Lucy* [1974]. This algorithm based on the Bayes' theorem on conditional probabilities is, for example, used in the sharpening of astronomical observations or underwater photography and is in the following used in the form

$$O_{i+1} = \left(\left(\frac{I}{O_i \otimes PSF} \right) \otimes PSF \right) O_i. \qquad (1)$$

The observed radiance field is I; O_i ($O_0 = I$) is the result of iteration step i, and PSF is the horizontal distribution of reflectivity generated by the MYSTIC "laser" simulation. The operator $\otimes$ is the convolution operator. Multiplications are point by point operations. The radiance field I is divided by a smoothed form $O_i \otimes PSF$ of itself. This high-pass filtering detects the sharp gradients of the field which are then, in a smoothed version, used to scale the result of the preceding iteration step O_i.

[22] A standard convolution operation $\otimes$ is equivalent to the sum of fields with each single point value spread out onto the surrounding points according to a smoothing kernel. This picture corresponds to the case of horizontal transport of photons in a cloud layer without gaps. An adjusted operator needs to be defined for broken cloud cases since the point spread function completely changes its shape at cloud edges. There the photon path lengths increase strongly and the probability to detect reflected photons close to their entry point into the cloud, as expected for the examples of point spread functions in Figure 6, would strongly decrease. Photons "lost" at cloud edges will increase the level of illumination for a large area of the cloud free part of the scene adjoining the cloud element, because of the large free horizontal path length. Thus the convolution operator is modified: After each convolution operation all values outside the cloud covered areas are averaged. This way the point spread function limiting the spread of reflection by horizontal photon transport to a small area is changed wherever cloud edges are approached: For the parts of the point spread function located outside the cloud area, the short rapidly decreasing tail of the function is

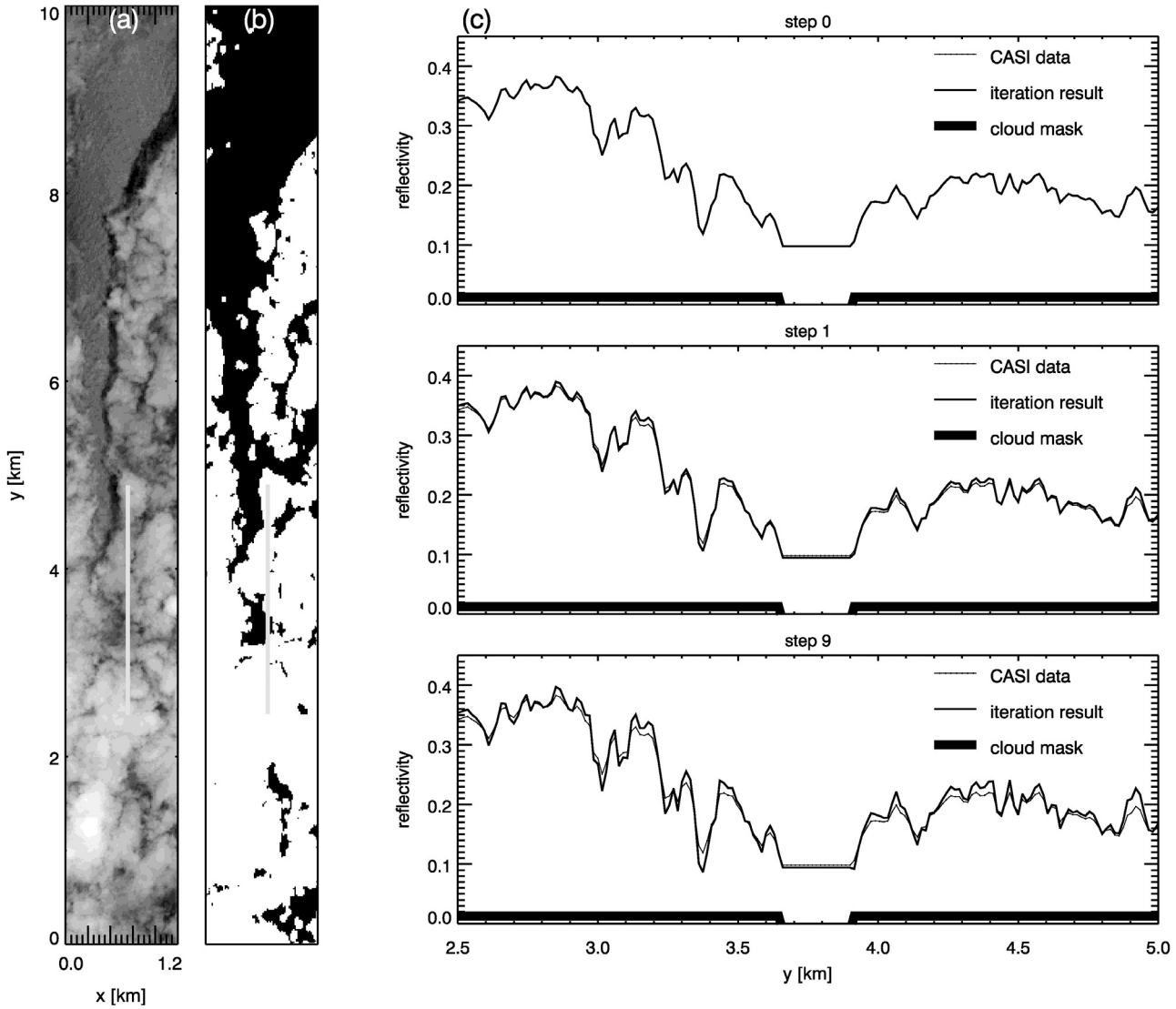

Figure 7. Richardson-Lucy algorithm for a CASI example: For the CASI observation (Figure 7a) a cloud mask (Figure 7b) is determined by means of a radiance threshold depending on solar zenith angle. For a 1-D section of the CASI data (Figure 7c) (marked with a gray line in Figures 7a and 7b) the effect of the algorithm on the radiance field is demonstrated for two iteration steps.

replaced by the value which would result if all lost photons were distributed equally over the cloud free scene. Of course, in reality not only the cloud free part but other cloud edges are illuminated by photon spread from neighboring clouds as well. However, the impact is much larger for the low reflective surface areas than for the bright cloud edges and, for the latter, the effect cannot be considered in a simplified qualitative way. The cloud mask used to classify cloudy pixels is implemented as a radiance threshold test for the original CASI observations (Figure 7). By each iterative deconvolution step the reflectivity of highly reflective cloud areas is increased as those areas have ''lost'' reflectivity by horizontal photon transport in the first place. On the contrary cloud free, low reflectivity, areas become darker through the iteration because they were illuminated diffusively by photon dispersion.

[23] This way, the adjusted Richardson-Lucy algorithm generates different versions of the observed reflectivity field with increasing sharpness. The cloud structures are obtained via the IPA retrieval of optical thickness and the adiabatic model, as mentioned above, assuming a fixed cloud base height determined from the shadows cast onto the sea surface for each observation date. In image processing such an iterative deconvolution procedure is often terminated before measurement noise is amplified. Here the iteration step will be selected for which the 3-D radiance simulation (and thus the underlying cloud structure) best matches the CASI observation (section 3.5).

3.4. Simulation of the Observation

[24] In principle, for each iteration step a 3-D MYSTIC simulation of reflectivity at 753 nm should be performed

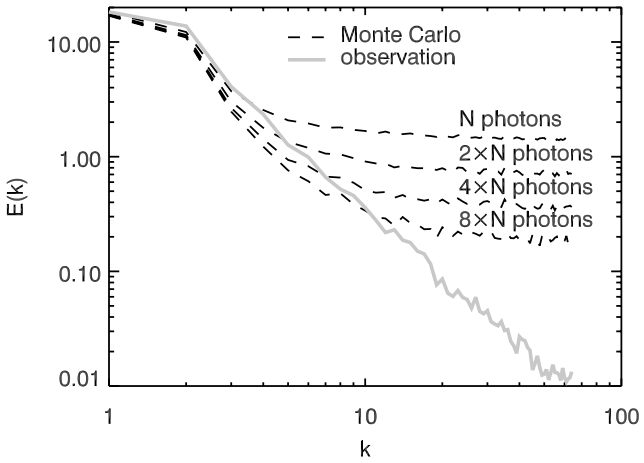

Figure 8. Power spectra of CASI reflectivity and Monte Carlo simulations with different numbers of photons. To obtain smooth power spectra, all available 1-D spectra of equal length along the x and y directions are averaged (true for all following spectra unless otherwise noted).

for the solar zenith angle at measurement time. Because of the high computational demand the extent of the trial simulations is restricted to the following: (1) The size of the simulation domain is confined to a section of the complete cloud structure of about 20% of the complete CASI scene, and (2) only the iteration steps 0 (representing the unchanged observation), 1, 2, 4, 6, 9, 12, and 15 are processed. The selection of an appropriate section from the whole cloud structure is optimized to meet the average values of optical thickness and cloud coverage typical for the specific scene as best as possible. The selection of iteration steps is motivated by the fact that the deconvolution algorithm converges quickly to the mathematical solution; that is, the step-to-step changes decrease.

3.5. Selection of Best Match

[25] This section describes the objective criteria to decide which of the eight trial simulations and their related cloud structures are the best match of the specific CASI observation. The most straightforward criterion is the point-by-point deviation of trial simulation and CASI observation. A small displacement of the maxima and minima due to the inclined illumination, however, would cause large differences when compared point by point. As one of the main concerns for the radiative transfer application is to obtain a realistic variability of the optical thickness field and the cloud top geometry, the power spectrum is a more appropriate criterion. An obstruction in the assessment of the variability is intrinsic to the Monte Carlo method itself. Although it lacks any approximations for the involved physical processes it is inescapably burdened with noise, i.e., with artificial small-scale variation. In Figure 8 the problem becomes obvious for the comparison of a power spectrum of a simulation and an observation. Especially at high frequencies, the Monte Carlo spectrum is dominated by noise. This is reduced only gradually with increasing number of photons and accordingly increasing computation time: The standard deviation of a sample mean, here the Monte Carlo simulation result, depends on the sample size, i.e., the number of photons N [*von Storch and Zwiers*, 1999]:

$$\sigma \propto \frac{1}{\sqrt{N}}. \tag{2}$$

In order to halve the uncertainty, 4 times more photons are required. Monte Carlo noise is white noise; that is, over all scales a constant noise amplitude is added (mind the logarithmic axes). Thus the Monte Carlo spectrum is difficult to compare to the observed spectrum. In the example shown, a large number of photons is required to demonstrate that the power spectrum of the simulated field actually drops faster than the observed spectrum in Figure 8. To keep the computational time in a feasible range, we developed a noise reduction technique: The total noise amplitude is determined and subtracted from the noisy spectrum. The amplitude is determined through several Monte Carlo runs with a low number of photons providing a confidence interval as well. A complete description of the denoising method is given in Appendix B.

[26] Figure 9 displays the basis for the selection for some of the trial cases: As mentioned in the beginning of this section, the primary criterion is the comparison of the power spectra of the trial simulations to the spectrum of the observation separately for the x and y directions (top panels in Figure 9); a secondary criterion is the direct comparison of the reflectivity fields. For the comparison of power spectra, the amplitudes are averaged over all scan lines, separately for the x and y directions. The directions are considered separately as the CASI simulation section has different side lengths. Therefore a higher weight is given to the longer y direction. The Fourier amplitudes of the simulations are compared to the ones of the observation by means of a root mean square deviation, if the standard deviation σ of the spectrum resulting from the noise removal does not exceed 10% of the amplitude (the confidence interval of 2σ is shown in the top panels of Figure 9). The reflectivity fields are compared by means of a root mean square deviation of the reflectivity values as well. The bottom left panel of Figure 9 shows the root-mean-square (RMS) deviations (part of the RMS deviation is caused by the Monte Carlo noise which amounts to about 2.5%). Three criteria of selection are used: The primary criterion is given by the level of agreement of the y direction power spectrum, secondary criteria are the agreement of the x power spectrum and the minimum RMS pixel deviation. For each of the criteria the best matching iteration step is selected. As the decision is not always as consistent as shown in the example Figure 9 (all criteria are in favor of step 4), a simple scoring algorithm is used to account for the hierarchy of the criteria. To the main criterion, the y direction power spectrum, the weight 3 is assigned. The weight 2 is given to each of the secondary criteria, x power spectrum and RMS pixel deviation. In this way an agreeing vote by the two secondary criteria would overrule the primary criterion.

[27] For broken cloud cases the differences between the iteration steps decrease with decreasing cloud cover. The selection of the exact iteration step is not decisive in these

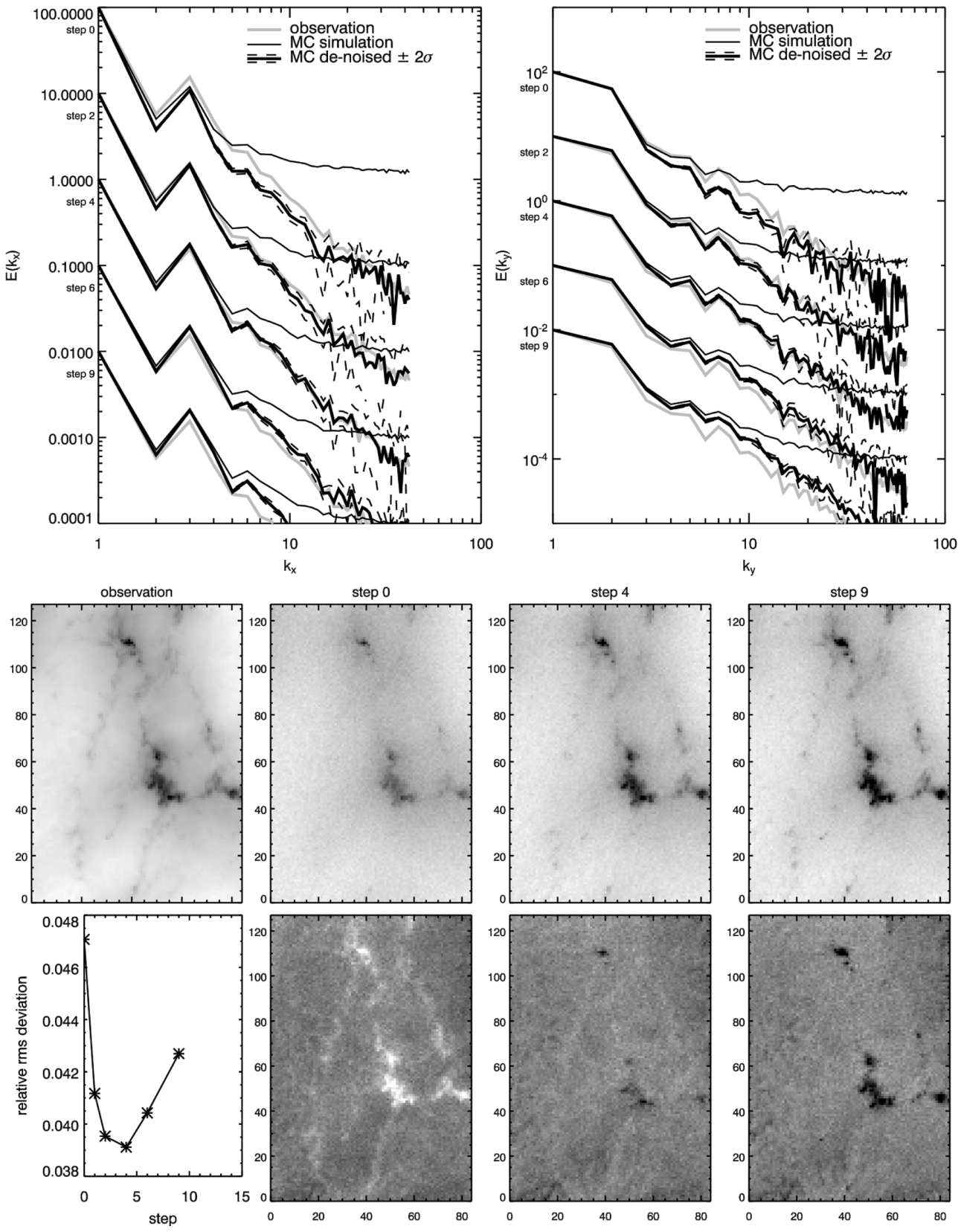

Figure 9. Example for the selection of the trial simulation matching the observation: (top) power spectra averaged along *x* and *y* axes for five cases, (middle) reflectivity of CASI observation and from Monte Carlo simulations, and (bottom) RMS deviation and related difference fields (white, simulation greater than observation; black, simulation less than observation).

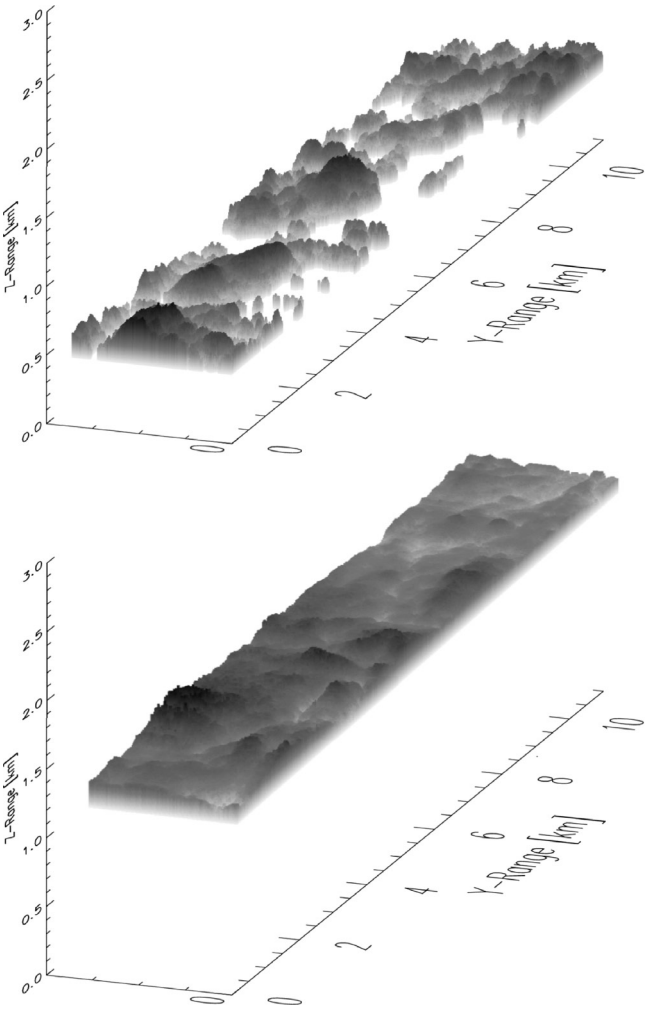

Figure 10. Results of the presented method: 3-D cloud structure for two CASI cases (compare Figure 1 and Figure 9). The gray scale clarifies the adiabatic vertical structure of the clouds (increasing LWC and droplet radius with height are indicated by darkening gray).

situations because the internal variation of the clouds becomes less important for the radiation field compared to the horizontal distribution pattern of cloudy areas.

[28] For all 27 cases iteration steps between 1 and 15 were selected. That means the unadjusted observation, step 0, was too smooth in all cases and the assumption that a sharpening by deconvolution leads to better approximations of the real cloud properties is valid. This situation changes for larger solar zenith angles (compare section 2.3). In that case, the sharpness introduced into the observation by the top geometry and the solar zenith angle dominates the smoothing effects. Thus it cannot be corrected for by a deconvolution because a further sharpening would only increase the differences.

[29] Figure 10 shows two of the 27 three-dimensional cloud structures obtained this way for the complete CASI scenes. Each data set has a spatial resolution of 15 m $\times$ 15 m $\times$ 10 m and a domain size of about 1.3 km $\times$ 10 km. Although the determined cloud structures are certainly not unambiguous, it is guaranteed that the simulated radiance field matches the initial observation.

3.6. Result Summary and Comparison to Other Measurements

[30] In this section the question if the obtained data set is representative for typical marine stratocumulus is addressed. Twenty-seven cloud structures with a cloud cover between 5 and 100% were obtained with the method presented in this paper. The range of the optical thickness is $0 < \tau < 40$ (average cloud optical thickness $\bar{\tau} = 9$) for a geometrical thickness h of up to 500 m ($\bar{h} = 146$ m). The effective radius reaches maximum values of 15 μm near the cloud top ($\overline{r_{eff}} = 9.4$ μm at cloud top). The variation of the cloud top height is characterized by standard deviations between 14 and 71 m depending on the cloud scene. Keeping in mind the limited number of cases the average numbers are in good agreement with the values measured in situ or via remote sensing techniques for the according dates of the ACE2 CLOUDYCOLUMN campaign [*Brenguier et al.*, 2000a; *Schüller et al.*, 2003]. The average value of LWP of 49 g/m^2, including about 35% cloudless columns (at a resolution of 15 m $\times$ 15 m), compares well to measurements of the LWP using microwave remote sensing during the Baltex Bridge Campaign (BBC) by *Crewell et al.* [2004]: For nonprecipitating stratocumulus under marine influence an average LWP of 42 g/m^2 was measured. Also the probability density function for the LWP observed during BBC on a comparable resolution (depending on the averaging time of the microwave sensor) closely resembles the PDF obtained for the CASI cloud structures (not shown). Similar probability density functions and mean values are found for data from other field campaigns like ASTEX or FIRE I [*Cahalan et al.*, 1995]. Hence we conclude that the derived data set is representative for marine stratocumulus clouds.

4. Test of the Method

[31] In this section the method will be tested for an a priori defined cloud structure. For this cloud a high-spatial-resolution radiance field is simulated using MYSTIC for a nadir viewing perspective corresponding to the CASI fields. Thus a synthetic observation is provided featuring all characteristics of a real CASI measurement, but in addition, in this case the underlying 3-D distribution of LWC and droplet radius is known and can be compared to the result obtained using the method presented in section 3.

[32] To allow the simulation of a synthetic observation with a Monte Carlo code which is accurate enough the simulation domain size is restricted to 1200 m $\times$ 1200 m. The cloud structure is taken from one of the CASI derived cloud data sets obtained in section 3. The simulation of the 3-D radiance distribution the CASI instrument would measure is done for a solar zenith angle of 5°, a nadir sensor view, and a horizontal resolution of 15 m $\times$ 15 m.

[33] In the same form as before, Figure 11 shows the selection criteria for this test case. All three criteria, i.e., the power spectrum in x and y directions and the RMS deviation from the synthetic observation, indicate iteration

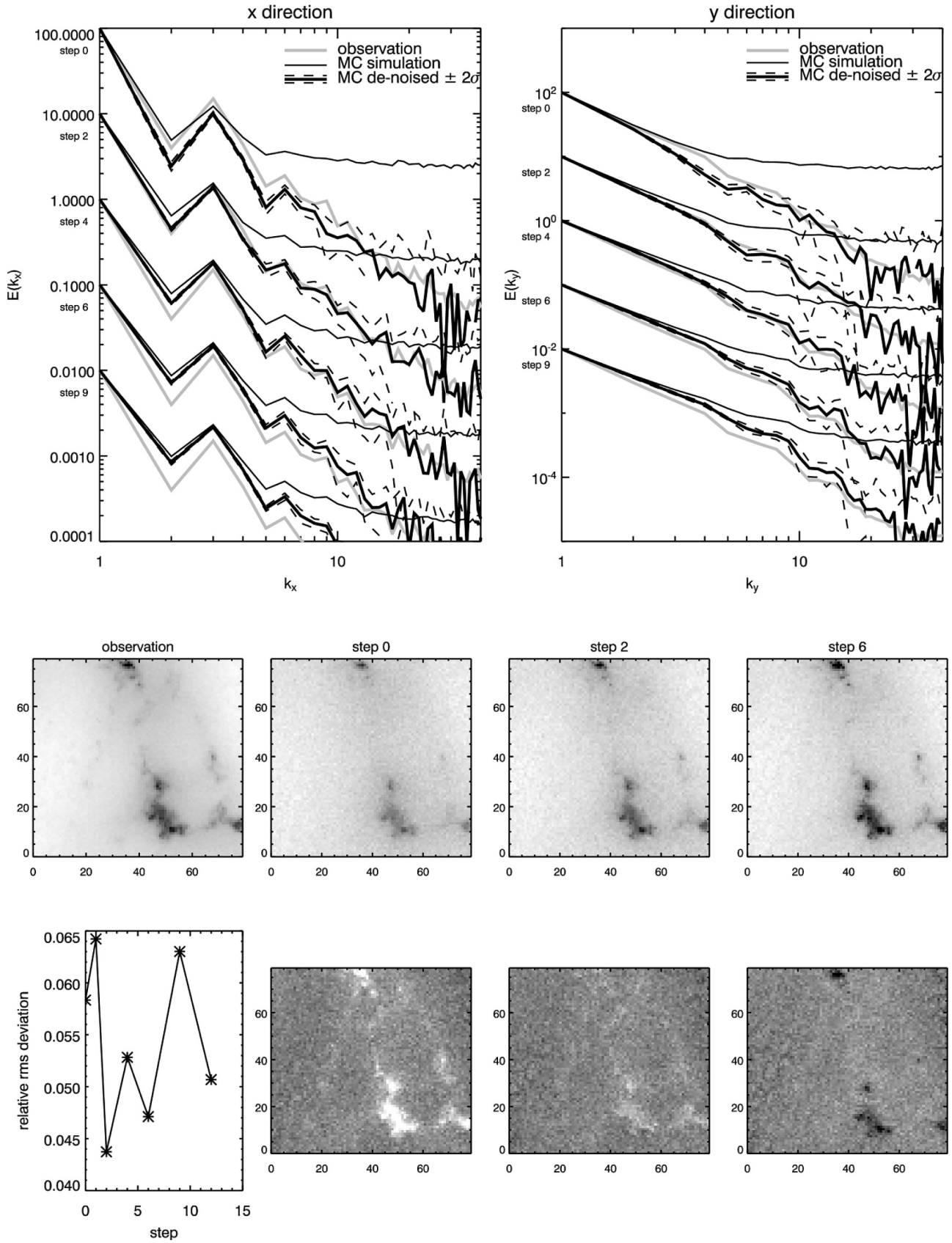

Figure 11. Test of method (compare Figure 9): In this example, the best match for the synthetic observation, simulated with the Monte Carlo model (middle left), is searched for.

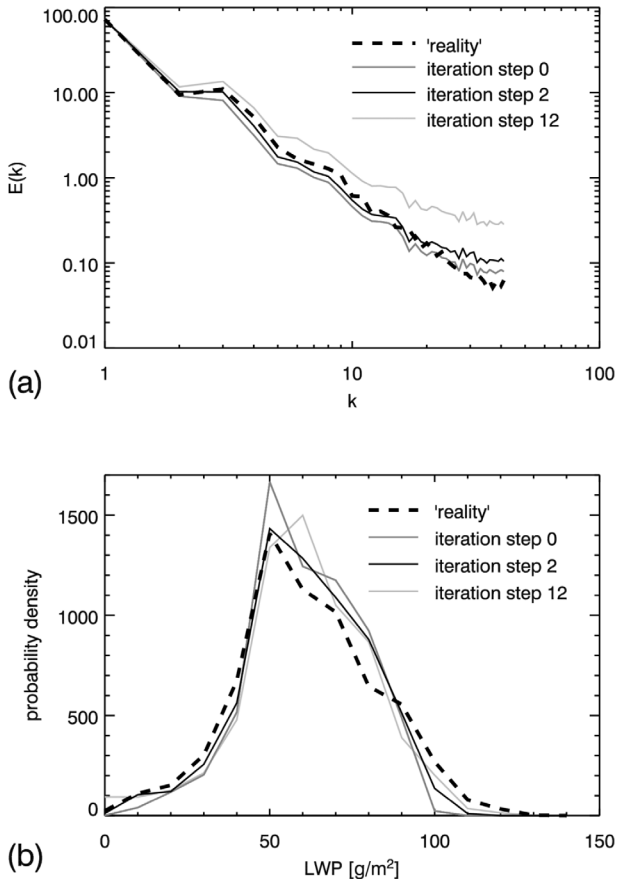

Figure 12. (a) Power spectrum and (b) probability density function for the distribution of LWP related to the "real" cloud structure and to several iteration steps of the method of section 3. Iteration step 0 reflects the typical problems of IPA remote sensing: underestimation of the variability and thus the narrowing of the PDF. Iteration step 2 obviously best matches the given synthetic cloud's values.

step 2 to be selected. This selection is confirmed by the analysis of the cloud structure derived from the synthetic observation shown in Figure 12. Both the Fourier spectrum and the probability density function (PDF) of the liquid water path field closely match the real underlying cloud's properties for iteration step 2. In contrast, the determination of a 3-D cloud structure without compensation of horizontal photon transport (iteration step 0) would result in a smoothed structure. Minimum and maximum values of LWP and consequently of effective radius and cloud top height would not be reached.

5. Discussion and Conclusions

[34] As mentioned before, the method might not produce unique solutions for each of the scenes. Other 3-D cloud structures are imaginable as well resulting in a correct reproduction of the initial measurements. However, as far as the original observation's viewing direction is concerned, it is guaranteed that the relevant 3-D radiative transfer processes are accounted for in a physical consistent way: Solid assumptions on the vertical characteristics link the horizontal distribution of optical properties to the vertical distribution; via accurate 3-D radiative transfer simulations the consistency of both distributions is checked against the original measurement. Because of this implicit cross-check, assumptions like the constant cloud bottom height or the exact characteristics of the adiabatic liquid water profile do have only minor impact on the result as far as radiative transfer investigations based on these cloud data are concerned. In the described manner the method is confined to small solar zenith angles, as otherwise large-scale shadows would distort the retrieved cloud scene and would make the basic idea of sharpening, unsmoothing the observation futile as in these cases the sharpening effects of horizontal transport dominates in the first place. A simplification is the use of one mean smoothing characteristic for the whole scene, which would in reality vary depending on local properties even without any sharpening or other interaction effects with the surrounding cloud areas.

[35] That means, under selected circumstances (small solar zenith angle, single layer stratocumulus) reliable horizontal cloud property distributions are determined on a high spatial resolution corrected for the dominant 3-D effects and a reasonable guess of their vertical structure and thus their cloud top geometry is provided. This way a number of 27 three-dimensional cloud structures representative of typical single layer marine stratocumulus is obtained directly related to a number of high-horizontal-resolution observations.

6. Outlook

[36] A method to derive 3-D cloud structures from high-resolution radiance data has been developed and applied to a representative set of marine stratocumulus observations. The computational effort is still large as several time consuming Monte Carlo simulations are involved. Further testing of the minimum number of photons to allow for the selection process (compare section 3 and Appendix B) can reduce computational time. The use of a backward Monte Carlo model, on the other hand, would allow for the simulation of a limited sample of independent lines of reflection (and their power spectra) for each scene and could thus either reduce the processing time as well or increase the representativeness of the results for large scenes without increasing the computational costs. A possible extension and speedup could be achieved by a precalculation of typical point spread functions based on a large number of combinations of optical and geometrical thicknesses. Such a table could then be used to extend the method from using a mean PSF for the deconvolution of the whole field to a deconvolution with a PSF fitting local properties. This step would certainly improve the retrieval of extreme values not reached yet (compare missing maximum values of LWP in Figure 12) and thus improve its applicability to other cloud types. Emphasis has been laid on accuracy rather than computational speed, hence the current method is too slow to be used as an operational technique. Nonetheless, it is an excellent possibility to derive cloud structures directly from measurements for systematic studies of inhomogeneity effects in radiative transport or for the experimental analysis of clouds during

field or satellite validation campaigns. For standard satellite cloud sensors (e.g., MODIS, AVHRR, Meteosat-SEVIRI) with a considerably larger pixel size the effects of horizontal photon transport discussed in this paper are of minor importance compared to the effects of unresolved subpixel-scale cloud inhomogeneity, at least unless the solar zenith angle is large or the pixel cloud cover is very small. The data set provided as a result here will be used for a systematic investigation of the impact of such subscale cloud inhomogeneity on remote sensing of cloud properties analyzing different typical cloud sensors in a follow-up publication [*Zinner and Mayer*, 2006].

Appendix A: Adiabatic Model for Cloud Microphysics

[37] The adiabatic water content describes the maximum amount of liquid water a cloud volume can contain assuming that the saturated cloud air parcel was lifted adiabatically from cloud base height, i.e., without exchange of heat with the surrounding air. During this ascent the air cools, the amount of water vapor decreases by condensation according to the decrease of the saturation water vapor pressure, the liquid water amount increases at the same rate, and the condensation heat reduces the vertical temperature lapse rate to the moist adiabatic lapse rate within the cloud. For boundary layer clouds the maximum value of adiabatic liquid water content is an approximation of the real conditions. Through entrainment of dry air into the cloud volume and other more dynamic cloud evolution effects the water content is changed. Nonetheless observational evidence for the adiabatic assumption has been found frequently [e.g., *Brenguier et al.*, 2000a; *Pawlowska et al.*, 2000].

[38] Starting point of the adiabatic model is an integrated value like a liquid water path or an optical thickness. By the adiabatic liquid water content which depends on height, the liquid water profile is defined and the cloud geometrical thickness results from the integrated value of the liquid water path.

[39] The saturated water vapor mixing ratio q_s (mass of water vapor per mass of dry air) is in good approximation given by

$$q_s = \varepsilon \frac{e_s}{p}, \tag{A1}$$

where e_s is the saturation vapor pressure, p is the atmospheric pressure, and $\varepsilon = 0.622$ is the ratio of the molecular masses of water and air. The saturation vapor pressure e_s only depends on the temperature and can be calculated using the Magnus equation [see, e.g., *Pruppacher and Klett*, 1997]. Executing dq_s/dz leads to the change of the water vapor mixing ratio and thus of liquid water depending on the change of temperature T with height, the moist adiabatic lapse rate $\Gamma_s = dT/dz$, and the change of air pressure with height $dp/dz = -\rho g$ (ρ: air density, g: gravitational acceleration). Using

$$\Gamma_s = -\frac{g}{c_p} \frac{1 - \rho L \left(\frac{dq_s}{dp}\right)_T}{1 + \frac{L}{c_p}\left(\frac{dq_s}{dT}\right)_p} \tag{A2}$$

(c_p, specific heat of dry air at constant pressure; L, latent heat of condensation; indices T and p designate the derivations at constant temperature and pressure, respectively [*Holton*, 1992]), dq_s/dz and thus the adiabatic liquid water content w_l above a certain cloud base height can be calculated as $w_l = q_s\rho$. For the shallow clouds investigated in this paper the values of pressure and temperature at an assumed cloud base height (taken from a standard atmosphere profile for midlatitude summer) are used to derive the adiabatic liquid water content.

[40] Assuming a fixed cloud droplet concentration N the effective radius can be determined according to

$$w_l = \frac{4}{3} \pi k r_{\text{eff}}^3 N \rho_w, \tag{A3}$$

where ρ_w is the density of water. The factor k represents the ratio r_v^3/r_{eff}^3 where r_v is the mean volume radius of a droplet spectrum. That means k depends on the specific shape of the droplet spectrum. From in situ measurements k is estimated to be between 0.67 ± 0.07 and 0.8 ± 0.07 for maritime or continental air masses, respectively [*Martin et al.*, 1994]. Here a value of 0.8 is used.

Appendix B: Denoising Power Spectra of Monte Carlo Simulations

[41] As shown in Figure 8 the power spectra of Monte Carlo simulated radiance fields are dominated by noise if the computational time is kept low enough to make the method feasible. The noise amplitude is about the same for all wave numbers but at high frequencies the influence is most obvious because the actual amplitude is smallest on these scales. Here a straightforward technique is presented to separate the spectrum of the solution from the noise spectrum: a simple subtraction of the noise amplitude.

[42] In real space as well as in Fourier space the Monte Carlo result is the sum of true result and noise. According to equation (2), doubling the number of photons decreases the noise level by the factor $\sqrt{2}$, according to a factor 2 in the power spectral quadratic amplitudes $A^2 = E(k)$. The complete power spectra A_N^2 and A_{8N}^2 of the $1 \times N$ photons and $8 \times N$ photons results can thus be written as the sum of the noise-free spectrum A^2 and the noise spectra A_σ^2 for N photons and accordingly $1/8\ A_\sigma^2$ for $8 \times N$ photons:

$$A_N^2 = A^2 + A_\sigma^2, \tag{B1}$$

$$A_{8N}^2 = A^2 + \frac{1}{8} A_\sigma^2. \tag{B2}$$

The difference in the quadratic amplitudes (Figure B1) between the two power spectra is then

$$\Delta A^2 = A_N^2 - A_{8N}^2 = \frac{7}{8} A_\sigma^2. \tag{B3}$$

To obtain the total noise spectrum A_σ^2, the difference spectrum ΔA^2 consequently has to be scaled by the factor 8/7.

[43] Then this scaled noise power spectrum can be subtracted from the Monte Carlo spectrum. Figure B1b shows the determination of the power spectrum of the $8 \times N$ Monte

Carlo run from 8 different $1 \times N$ runs allowing not only to obtain the $8 \times N$ run's spectrum but also to define a confidence interval. The interval is given by the standard deviation (2σ) for the quadratic amplitude at each wave number. In the same way the scaled difference spectrum leads to a completely "denoised" spectrum (Figure B1c).

[44] Figure B2 shows a demonstration of the technique using a predefined field of values and its power spectrum. To this test field Gaussian noise is added to result in eight different noisy versions of the "truth," the equivalent to eight "Monte Carlo simulations." As before the difference in noise amplitude between the eight single fields and their mean (equivalent to the $8 \times N$ Monte Carlo simulation) is determined and, after the scaling step, removed from the 8 single power spectra. The true noise free power spectrum is almost perfectly reproduced.

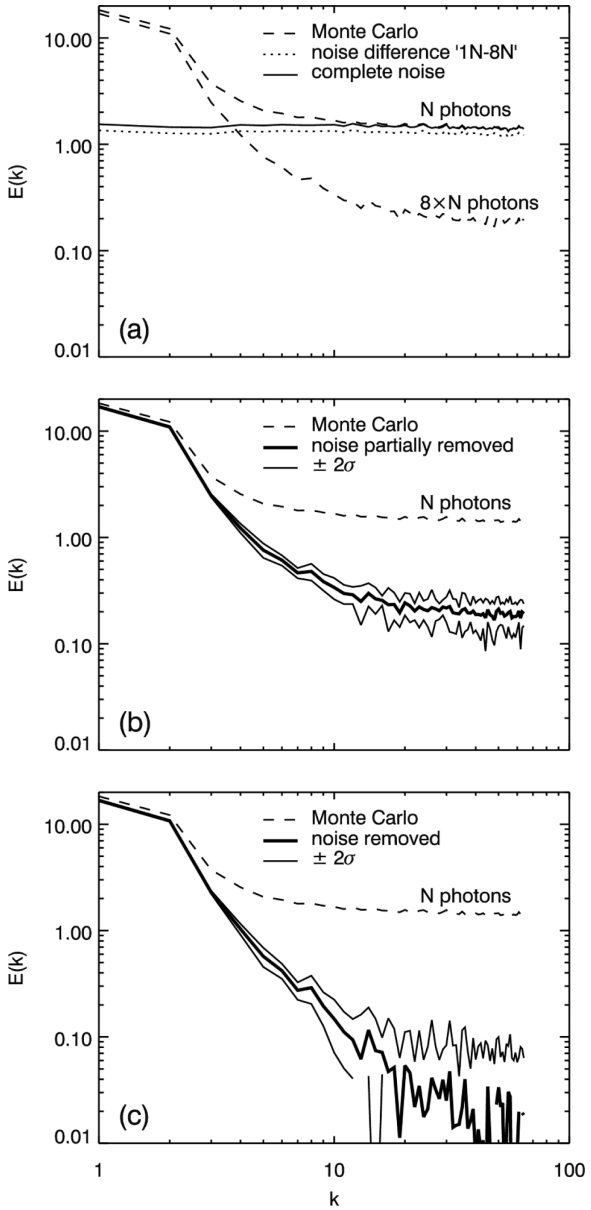

Figure B1. (a) Power spectra for different numbers of photons: $1 \times N$ and $8 \times N$. The difference in quadratic amplitude is due to Monte Carlo noise. The complete noise spectrum is determined by scaling the difference spectrum. (b) Determination of $8 \times N$ spectrum through the subtraction of difference spectrum from $1 \times N$ spectra. (c) Complete removal of quadratic noise amplitude from spectrum using the scaled noise spectrum (compare Figure B1a).

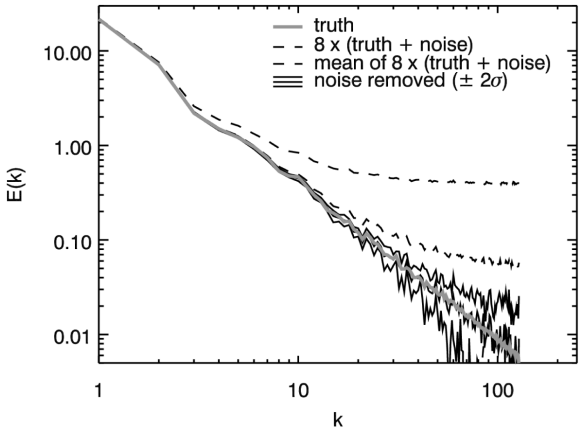

Figure B2. Demonstration of noise removal technique: Starting from a known "truth," eight noisy versions are obtained. The noise level is determined and removed (compare Figure B1). The true spectrum is reproduced.

[45] It should be pointed out that this technique only allows the removal of the noise influence in the power spectrum. A back transformation into real space is of course not possible as the phases cannot be corrected for the noise influence.

[46] **Acknowledgments.** Tobias Zinner was supported by the EC-funded CLOUDMAP project, EVK2-2000-00547. The authors thank Andreas Macke and an anonymous reviewer for their constructive comments.

References

Anderson, G., S. Clough, F. Kneizys, J. Chetwynd, and E. Shettle (1986), AFGL atmospheric constituent profiles, *AFGL Tech. Rep., AFGL-TR-86-0110*.

Babey, S., and C. Anger (1989), A compact airborne spectrographic imager (CASI), paper presented at IGARSS, Inst. of Electr. and Electron. Eng., Vancouver, B. C., Canada.

Barker, H. W., R. K. Goldstein, and D. E. Stevens (2003), Monte Carlo simulation of solar reflectances for cloudy atmospheres, *J. Atmos. Sci.*, *60*, 1881–1894.

Brenguier, J.-L., H. Pawlowska, L. Schüller, R. Preusker, J. Fischer, and Y. Fouquart (2000a), Radiative properties of boundary layer clouds: Droplet effective radius versus number concentration, *J. Atmos. Sci.*, *57*, 803–821.

Brenguier, J.-L., et al. (2000b), An overview of the ACE-2 CLOUDY-COLUMN closure experiment, *Tellus, Ser. B*, *52*, 815–827.

Bryan, G. H., J. C. Wyngaard, and J. M. Fritsch (2003), Resolution requirements for the simulation of deep moist convection, *Mon. Weather Rev.*, *131*(10), 2394–2416.

Cahalan, R. F., W. Ridgway, W. J. Wiscombe, and T. L. Bell (1994a), The albedo of fractal stratocumulus clouds, *J. Atmos. Sci.*, *51*, 2434–2455.

Cahalan, R. F., W. Ridgway, W. J. Wiscombe, S. Gollmer, and Harshvardhan (1994b), Independent pixel and Monte Carlo estimates of stratocumulus albedo, *J. Atmos. Sci.*, *51*, 3776–3790.

Cahalan, R. F., D. Silberstein, and J. Snider (1995), Liquid water path and plane-parallel albedo bias during ASTEX, *J. Atmos. Sci.*, *52*, 3002–3012.

Cahalan, R. F., et al. (2005), The International Intercomparison of 3D Radiation Codes (I3RC): Bringing together the most advanced radiative transfer tools for cloudy atmospheres, *Bull. Am. Meteorol. Soc.*, *86*, 1275–1293.

Chuang, P. Y. (2000), CCN measurements during ACE-2 and their relationship to cloud microphysical properties, *Tellus, Ser. B*, *52*, 843–867.

Coakley, J. A., Jr. (1991), Reflectivities of uniform and broken layered clouds, *Tellus, Ser. B*, *43*, 420–433.

Crewell, S., et al. (2004), The BALTEX Bridge Campaign: An integrated approach for a better understanding of clouds, *Bull. Am. Meteorol. Soc.*, *85*, 1565–1584, doi:10.1175/BAMS-85-10-1565.

Davis, A., A. Marshak, R. Cahalan, and W. Wiscombe (1997), The Landsat scale break in stratocumulus as a three-dimensional radiative transfer effect: Implications for cloud remote sensing, *J. Atmos. Sci.*, *54*, 241–260.

Davis, A. B., R. F. Cahalan, D. Spinhirne, M. J. McGill, and S. P. Love (1999), Off-beam Lidar: An emerging technique in cloud remote sensing based on radiative Green-function theory in the diffusion domain, *Phys. Chem. Earth B: Hydrol. Oceans Atmos.*, *24*(3), 177–185.

Di Giuseppe, F., and A. M. Tompkins (2003), Effect of spatial organization on solar radiative transfer in three-dimensional idealized stratocumulus cloud fields, *J. Atmos. Sci.*, *60*, 1774–1794.

Evans, K. F., and W. J. Wiscombe (2004), An algorithm for generating stochastic cloud fields from radar profile statistics, *Atmos. Res.*, *72*, 263–289.

Faure, T., H. Isaka, and B. Guillemet (2001), Neural network retrieval of cloud parameters of inhomogeneous and fractional clouds. Feasibility study, *Remote Sens. Environ.*, *77*, 123–138.

Faure, T., H. Isaka, and B. Guillemet (2002), Neural network retrieval of cloud parameters from high-resolution multispectral radiometric data: A feasibility study, *Remote Sens. Environ.*, *80*, 285–296.

Fu, Q., M. Cribb, H. Barker, S. Krueger, and A. Grossman (2000), Cloud geometry effects on atmospheric solar absorption, *J. Atmos. Sci.*, *57*, 1156–1168.

Holton, J. R. (1992), *An Introduction to Dynamic Meteorology*, *Int. Geophys. Ser.*, vol. 48, Elsevier, New York.

Iwabuchi, H., and T. Hayasaka (2003), A multi-spectral non-local method for retrieval of boundary layer cloud properties from optical remote sensing data, *Remote Sens. Environ.*, *88*, 294–308.

Kolmogorov, A. N. (1941), Local structure of turbulence in incompressible viscous fluid at a very high Reynolds number, *Dokl. Akad. Nauk. SSSR*, *30*, 299–302.

Loeb, N. G., T. Varnai, and D. M. Winker (1998), Influence of subpixel-scale cloud-top structure of reflectances from overcast stratiform cloud layers, *J. Atmos. Sci.*, *55*, 2960–2973.

Lucy, L. B. (1974), An iterative technique for the rectification of observed distributions, *Astron. J.*, *79*, 745–754.

Marshak, A., A. Davis, W. Wiscombe, and R. Cahalan (1995), Radiative smoothing in fractal clouds, *J. Geophys. Res.*, *100*(D12), 26,247–26,261.

Marshak, A., A. Davis, R. Cahalan, and W. Wiscombe (1998a), Nonlocal independent pixel approximation: Direct and inverse problems, *IEEE Trans. Geosci. Remote Sens.*, *36*, 192–204.

Marshak, A., A. Davis, W. Wiscombe, and R. Cahalan (1998b), Radiative effects of sub-mean free path liquid water variability observed in stratiform clouds, *J. Geophys. Res.*, *103*(D16), 19,557–19,567.

Marshak, A., A. Davis, W. Wiscombe, W. Ridgway, and R. Cahalan (1998c), Biases in shortwave column absorption in the presence of fractal clouds, *J. Clim.*, *11*, 431–446.

Martin, G. M., D. W. Johnson, and A. Spice (1994), The measurement and parameterization of effective radius of droplets in warm stratocumulus clouds, *J. Atmos. Sci.*, *51*, 1823–1842.

Mayer, B. (1999), I3RC phase 1 results from the MYSTIC Monte Carlo model, in *Intercomparison of Three-Dimensional Radiation Codes: Abstracts of the First and Second International Workshops*, pp. 49–54, Univ. of Ariz. Press, Tucson.

Mayer, B. (2000), I3RC phase 2 results from the MYSTIC Monte Carlo model, in *Intercomparison of Three-Dimensional Radiation Codes: Abstracts of the First and Second International Workshops*, pp. 107–108, Univ. of Ariz. Press, Tucson.

Mayer, B., and A. Kylling (2005), Technical note: The libRadtran software package for radiative transfer calculations: Description and examples of use, *Atmos. Chem. Phys.*, *5*, 1855–1877.

O'Hirok, W., and C. Gautier (1998), A three-dimensional radiative transfer model to investigate the solar radiation within a cloudy atmosphere. Part I: Spatial effects, *J. Atmos. Sci.*, *55*, 2162–2179.

Pawlowska, H., J.-L. Brenguier, and F. Burnet (2000), Microphysical properties of stratocumulus clouds, *Atmos. Res.*, *55*, 15–33.

Pruppacher, H. R., and J. D. Klett (1997), *Microphysics of Clouds and Precipitation*, Springer, New York.

Richardson, W. H. (1972), Bayesian-based iterative method of image restoration, *J. Opt. Soc. Am.*, *62*, 55–59.

Rossow, W. B., C. Delo, and B. Cairns (2002), Implications of the observed mesoscale variations of clouds for the Earth's radiation budget, *J. Clim.*, *15*, 557–585.

Scheirer, R., and A. Macke (2003), Cloud inhomogeneity and broadband solar fluxes, *J. Geophys. Res.*, *108*(D19), 4599, doi:10.1029/2002JD003321.

Scheirer, R., and S. Schmidt (2005), CLABAUTAIR: A new algorithm for retrieving three-dimensional cloud structure from airborne microphysical measurements, *Atmos. Chem. Phys.*, *5*, 2333–2340.

Schröder, M., and R. Bennartz (2003), Impact of gas absorption and surface albedo on cloud radiative smoothing, *Geophys. Res. Lett.*, *30*(4), 1168, doi:10.1029/2002GL016523.

Schüller, L., J.-L. Brenguier, and H. Pawlowska (2003), Retrieval of microphysical, geometrical, and radiative properties of marine stratocumulus from remote sensing, *J. Geophys. Res.*, *108*(D15), 8631, doi:10.1029/2002JD002680.

Stephens, G., et al. (2002), The Cloudsat mission and the A-train, *Bull. Am. Meteorol. Soc.*, *83*, 1771–1790.

Varnai, T. (2000), Influence of three-dimensional radiative effects on the spatial distribution of shortwave cloud reflection, *J. Atmos. Sci.*, *57*, 216–229.

Varnai, T., and A. Marshak (2001), Statistical analysis of the uncertainties in cloud optical depth retrievals caused by three-dimensional radiative effects, *J. Atmos. Sci.*, *58*, 1540–1548.

Venema, V., S. Meyer, S. G. Garcia, C. Simmer, S. Crewell, U. Löhnert, and T. Trautmann (2004), Iterative amplitude adapted Fourier transform surrogate cloud fields, paper presented at 14th International Conference on Clouds and Precipitation, World Meteorol. Organ., Bologna, Italy.

von Storch, H., and F. W. Zwiers (1999), *Statistical Analysis in Climate Research*, Cambridge Univ. Press, New York.

Wyser, K., W. O'Hirok, C. Gautier, and C. Jones (2002), Remote sensing of surface solar irradiance with corrections for 3-D cloud effects, *Remote Sens. Environ.*, *80*, 272–284.

Zinner, T., and B. Mayer (2006), Remote sensing of stratocumulus clouds: Uncertainties and biases due to inhomogeneity, *J. Geophys. Res.*, doi:10.1029/2005JD006955, in press.

B. Mayer and T. Zinner, Institut für Physik der Atmosphäre, Deutsches Zentrum für Luft- und Raumfahrt Oberpfaffenhofen, Münchner Straße 20, D-82230 Weßling, Germany. (tobias.zinner@dlr.de)

M. Schröder, Institut für Weltraumwissenschaften, Fachbereich Geowissenschaften (FB 24), Freie Universität Berlin, Carl-Heinrich-Becker-Weg 6-10, D-12165 Berlin, Germany.